

# Task-Aware Dynamic Transformer for Efficient Arbitrary-Scale Image Super-Resolution

Tianyi Xu<sup>a</sup>, Yijie Zhou<sup>a</sup>, Xiaotao Hu<sup>b</sup>, Kai Zhang<sup>c</sup>, Anran Zhang<sup>d</sup>, Xingye Qiu<sup>e,f</sup> and Jun Xu<sup>a,g,\*</sup>

<sup>a</sup> School of Statistics and Data Science, Nankai University, Tianjin, China

<sup>b</sup> College of Computer Science, Nankai University, Tianjin, China

<sup>c</sup> School of Intelligence Science and Technology, Nanjing University, Suzhou, China

<sup>d</sup> Tencent Data Platform, Beijing, China

<sup>e</sup> Zhejiang University, Hangzhou, China

<sup>f</sup> Systems Engineering Research Institute, China State Shipbuilding Corporation Limited, Beijing, China

<sup>g</sup> Guangdong Provincial Key Laboratory of Big Data Computing, The Chinese University of Hong Kong, Shenzhen, China

**Abstract.** Arbitrary-scale super-resolution (ASSR) aims to learn a single model for image super-resolution at arbitrary magnifying scales. Existing ASSR networks typically comprise an off-the-shelf scale-agnostic feature extractor and an arbitrary scale upsampler. These feature extractors often use fixed network architectures to address different ASSR inference **tasks**, each of which is characterized by an **input image** and an **upsampling scale**. However, this overlooks the difficulty variance of super-resolution on different inference scenarios, where simple images or small SR scales could be resolved with less computational effort than difficult images or large SR scales. To tackle this difficulty variability, in this paper, we propose a Task-Aware Dynamic Transformer (TADT) as an input-adaptive feature extractor for efficient image ASSR. Our TADT consists of a multi-scale feature extraction backbone built upon groups of Multi-Scale Transformer Blocks (MSTBs) and a Task-Aware Routing Controller (TARC). The TARC predicts the inference paths within feature extraction backbone, specifically selecting MSTBs based on the input images and SR scales. The prediction of inference path is guided by a new loss function to trade-off the SR accuracy and efficiency. Experiments demonstrate that, when working with three popular arbitrary-scale upsamplers, our TADT achieves state-of-the-art ASSR performance when compared with mainstream feature extractors, but with relatively fewer computational costs. The code is available at <https://github.com/Tillyhere/TADT>.

## 1 Introduction

The goal of Arbitrary-Scale Super-Resolution (ASSR) is to learn a single model capable of performing image super-resolution at arbitrary scales [18, 9, 42, 50]. Current ASSR methods [18, 9, 4, 27] primarily focus on developing arbitrary-scale upsamplers to predict the high-resolution (HR) image from the feature of a low-resolution (LR) image extracted by an off-the-shelf feature extractor [31, 54, 30]. Inspired by the merits of meta-learning [13], the work of MetaSR [18] learns adaptive upsamplers according to the SR scale. Later, the methods of [9, 50, 27, 6] leverage the implicit neural representation [10] to predict the upsampled HR image by the coordinates and the feature

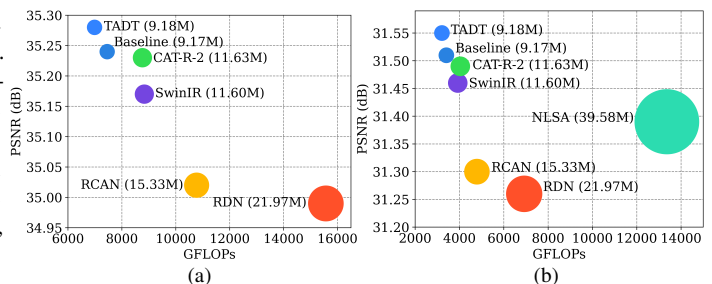


**Figure 1.** PSNR results, GFLOPs and parameter amounts of different feature extractors working with the upsampler LIIF [9] for (a)  $\times 2$  super-resolution and (b)  $\times 3$  super-resolution on the DIV2K validation set [1]. The disc radius is proportional to parameter amounts of different feature extractors. Baseline and TADT are our feature extractors that will be introduced in §3.3.

map of the corresponding LR image. However, feature extractors [31, 54, 30] in these ASSR methods are usually scale-agnostic, which discourage the adaptivity of extracted feature map to the multiple user-defined SR scale and leads to inferior SR results [42, 14].

To extract scale-aware feature for image ASSR, some researchers attempt to design scale-conditional convolutions to dynamically generate scale-aware filters [42, 14, 46]. For example, ArbSR [42] employs scale-aware convolution which fuses a set of filters using weights dynamically generated based on the scale information. The method of EQSR [46] achieves adaptive modulation of convolution kernels with scale-aware embedding. Implicit Diffusion Model [14] presents a scale-aware mechanism to work with a denoising diffusion model for high-fidelity image ASSR. In short, these methods mainly implement feature-level or parameter-level modulation mechanisms for scale-aware feature extraction. However, these feature extractors tackle the input images and SR scales of different difficulty by fixed network architectures. This inevitably emerges huge computational redundancy in “easy” inference scenarios, *e.g.*, “simple” images and/or small SR scales, that can be effectively resolved with less computational effort.

The variability of restoring difficulty on different images is inherent in image restoration [26]. It is more evident for image ASSR, since the difficulty variance of ASSR comes from not only content-diverse input images, but also different upsampling scales. On one hand, content-diverse images often suffer from different restoration difficulty and

\* Corresponding Author. Email: csjunxu@nankai.edu.cn

require image-adaptive inference complexity [26, 19]. On the other, the difficulty variability of image ASSR emerges as higher upsampling scales usually need larger computational burden [2]. Considering an input image and the corresponding upsampling scale factor as an ASSR task, it is essential to develop task-aware feature extractors with adaptive inference based on the difficulty of ASSR tasks.

For this goal, in this work, we propose the Task-Aware Dynamic Transformer (TADT) as an efficient feature extractor, with dynamic computational graphs upon different ASSR tasks. Specifically, our feature extractor TADT has a feature extraction backbone and a Task-Aware Routing Controller (TARC). The backbone contains multiple Multi-Scale Transformer Blocks (MSTBs) to exploit multi-scale representation [29, 51, 52]. Our TARC predicts the inference path of the backbone for each ASSR task, realizing task-aware inference with dynamic architectures. It is a two-branch module to transform the input image and SR scale into a probability vector and an intensity indicator respectively. The probability vector is modulated by the intensity indicator to produce the sampling probability vector, which is used to predict the final routing vector by Bernoulli Sampling combined with the Straight-Through Estimator [3, 24]. The routing vector determines the computational graph of the feature extraction backbone in our TADT to make it aware of input images and scales for image ASSR.

To make TADT more efficient, we further design a loss function to penalize the intensity indicator. Experiments on ASSR demonstrate that, TADT outperforms mainstream feature extractors by fewer parameter amounts and computation costs, and better ASSR performance when working with arbitrary-scale upsamplers of MetaSR [18], LIIF [9], and LTE [27] (a glimpse is provided in Figure 1).

Our main contributions can be summarized as follows:

- We propose the Task-Aware Dynamic Transformer (TADT) as a new feature extractor for efficient image ASSR. The main backbone of our TADT is built upon cascaded multi-scale transformer blocks (MSTBs) to learn expressive feature representations.
- We develop a task-aware routing controller to predict adaptive inference paths within the main backbone of TADT feature extractor for different ASSR tasks defined by the input image and SR scale.
- We devise an intensity loss function to guide the prediction of inference paths in our feature extraction backbone, leading to efficient image ASSR performance.

## 2 Related Work

### 2.1 Arbitrary-Scale Image Super-Resolution

Arbitrary-Scale Super-Resolution (ASSR) methods learn a single SR model to tackle the image super-resolution of arbitrary scale factors [18]. Meta-SR [18] represents one of the earliest endeavors in image ASSR, which dynamically predicts weights of filters for different scales by the meta-upscale module inspired by the meta-learning scheme [13]. Then, LIIF [9] pioneers local implicit neural representation for continuous image upsampling. Following this direction, Ultra-SR [49] integrates spatial encoding with implicit image function to improve the recovery of high-frequency textures. LTE [27] transforms the spatial coordinates into the Fourier frequency domain and learns implicit representation for detail enhancement. Attention [40] is also exploited in the methods of ITSRN, Ciao-SR [4] and CLIT [6]. These methods mainly focus on designing scale-aware upsamplers, but often employ input-agnostic feature extractors [31, 54, 30] leading to inferior image ASSR performance [42, 5, 46].

To mitigate this, recent ASSR methods [42, 5, 46] incorporate scale information into the feature extractors. ArbSR [42] and EQSR [46] dynamically predicts filter weights from scale-conditioned feature

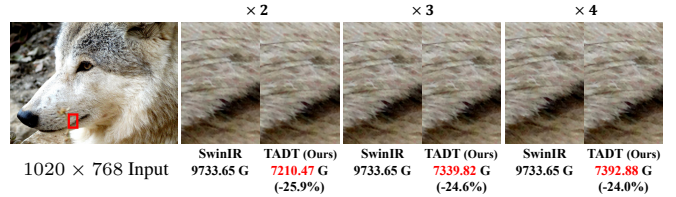


**Figure 2. Computational FLOPs of SwinIR [30] and our TADT on one image from DIV2K at different SR scales.** The arbitrary-scale upsampler is LIIF [9]. Our TADT uses less computational costs for smaller SR scales. Differently, LISR [5] and IDM [14] learn scale-conditioned attention weights to modulate scale-aware feature channels. These methods mainly extract scale-aware feature by feature or parameter level modulation, but with fixed inference architectures. This still limits their efficiency to tackle the versatile images and SR scale factors in ASSR. In this work, we propose a hyper-network [16] as the feature extractor that is aware of both the image and scale to achieve dynamic ASSR inference with adaptive computational efficiency.

### 2.2 Dynamic Networks

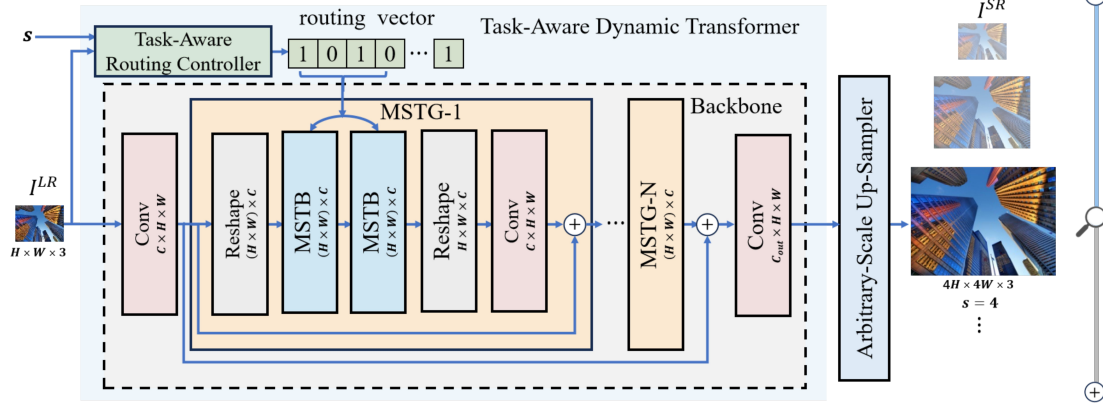
The dynamic inference is explored mainly from three aspects for expressive representation power and adaptive inference efficiency [17]: spatially-adaptive [8, 7], temporal-adaptive [47, 15, 41], and sample-adaptive [45]. By taking input image and SR scale as an inference sample, our Task-Aware Dynamic Transformer (TADT) based ASSR network belongs to the category of sample-adaptive dynamic inference. Sample-adaptive dynamic networks have been developed mainly to learn dynamic parameters or architectures [17]. Parameter-dynamic methods [12, 35] only tailor the network parameters according to the input, but under fixed network architectures. Architecture-dynamic methods mainly perform inference from three aspects: dynamic depth [21], dynamic width [28, 25], and dynamic routing [33, 56]. The depth-dynamic inference mainly resort to early exiting [17] or layer skipping [45]. The width-dynamic inference [28, 25] typically leverage dynamic channel or neuron pruning techniques [32]. Dynamic inference routing is usually employed to learn sample-specific inference architecture [33, 56]. In this work, we develop a transformer-based multi-branch feature extractor, and arm it with a task-aware network routing controller for architecture-dynamic image ASSR inference.

## 3 Methodology

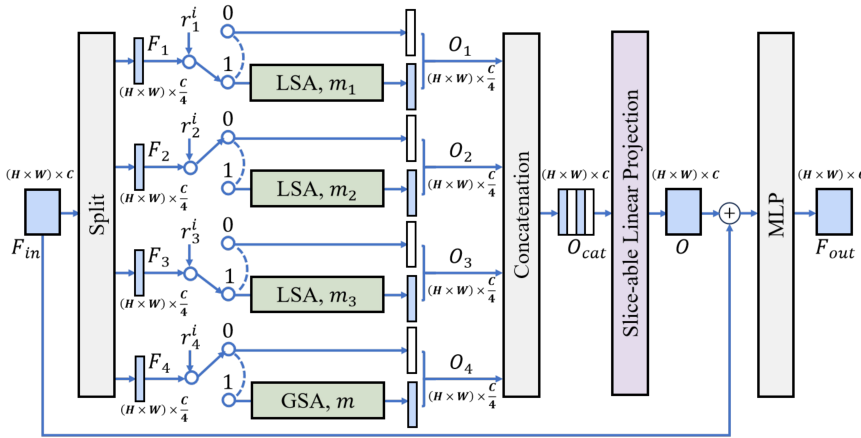
### 3.1 Motivation

Scale-agnostic feature extractors for ASSR consume the same computation overhead for super-resolution of different images or scales, and ignore the variance of super-resolution difficulty for diverse ASSR tasks (input images and SR scales) [2]. This brings computational redundancy to these feature extractors upon relatively “easy” ASSR tasks. To illustrate this point, in Figure 2, we compare the SR images of LIIF [9] using SwinIR [30] or our method (will be introduced later) as the feature extractor on one 1020 × 768 image from the DIV2K dataset. One can see that SwinIR needs a constant FLOPs of 9733.65G to extract features for ASSR task with SR scales of ×2, ×3, and ×4. On the contrary, our TADT needs less computational costs for SR tasks of lower scales, and enables LIIF [9] to output SR images with similar or even better image quality than those of SwinIR. In the end, it is promising to develop a feature extractor with dynamic computational graphs for image ASSR, which is the main motivation of our work. Next, we will elaborate our method for image ASSR.

(a) Architecture of Our ASSR Network



(b) Multi-Scale Transformer Block (MSTB)



(c) Task-Aware Routing Controller

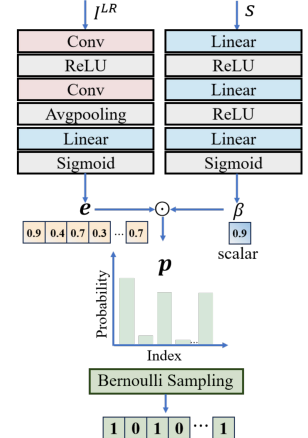


**Figure 3. Illustration of our ASSR network.** (a) Architecture of our ASSR network containing our Task-Aware Dynamic Transformer and an arbitrary-scale upsampler. (b) Our Multi-scale Transformer Block (MSTB). “LSA” indicates local self-attention with a window size of  $m_j$  for the  $j$ -th branch. “GSA” indicates global self-attention with a window size of  $m$ . (c) Our Task-Aware Routing Controller is a two-branch module aware of the input image  $I^{LR}$  and SR scale  $s$ .

### 3.2 Network Overview

The overall pipeline of our ASSR network is illustrated in Figure 3 (a). It takes our Task-Aware Dynamic Transformer (TADT) as the feature extractor and an arbitrary-scale upsampler to output the magnified image. Our TADT extractor comprises a main multi-scale feature extraction backbone and a Task-Aware Routing Controller (TARC). The feature extraction backbone first utilizes a convolution layer to obtain the shallow feature. It then learns scale-aware deep feature, with the routing vector provided by our TARC, by  $N$  cascaded Multi-Scale Transformer Groups (MSTGs) appended by a convolution layer. Each MSTG group contains two Multi-Scale Transformer Blocks (MSTBs) and a convolution layer, and each MSTB learns multi-scale representation by four self-attention branches. A skip connection is used to fuse the shallow feature and the extracted feature by  $N$  MSTG groups. Our TARC controller predicts the routing vector of our TADT feature extraction backbone, *i.e.*, the selection of self-attention branches, for different input LR images and SR scales. More detailed structure of our TADT will be presented in §3.3.

For the arbitrary-scale upsampler, we employ the off-the-shelf methods such as MetaSR [18], LIIF [9], and LTE [27], *etc.*

### 3.3 Proposed Task-Aware Dynamic Transformer

In this work, we propose a task-aware feature extractor based on transformers [30, 52] for image ASSR. The proposed extractor can adjust its computational graph according to different LR images and upsampling scales, to achieve dynamic feature extraction with adaptive

computational costs. Since each set of input LR image and upsampling scale constitute the inputs of an inference task in ASSR, our feature extractor is termed as Task-Aware Dynamic Transformer (TADT).

Given an inference task consisting of an LR image  $I^{LR}$  and an upsampling scale factor  $s$ , our Task-Aware Routing Controller (TARC) first predicts a binary routing vector  $\mathbf{r} \in \{0, 1\}^{4N}$ . Here,  $4N$  is the number of controllable self-attention branches in the feature extraction backbone, since each MSTB block has four self-attention branches and the two MSTBs in each MSTG group use the same branches. The backbone then encodes the LR image  $I^{LR}$  of an input task and determine its computational graph according to the routing vector  $\mathbf{r}$ . Specifically, the routing vector  $\mathbf{r}$  consists of  $N$  sets of 4-dimensional routing sub-vectors as  $\mathbf{r} = [\mathbf{r}^1, \dots, \mathbf{r}^i, \dots, \mathbf{r}^N]$ , where  $\mathbf{r}^i = [r_1^i, r_2^i, r_3^i, r_4^i]$ . Here,  $\mathbf{r}^i$  ( $i = 1, \dots, N$ ) is the sub-vector of the  $i$ -th MSTG and  $r_j^i = 0$  or  $1$  ( $j \in \{1, 2, 3, 4\}$ ) is the routing index of the  $j$ -th self-attention branch.  $r_j^i = 1$  means that the  $j$ -th branch of two MSTBs in the  $i$ -th MSTG is used. Otherwise, this branch will be bypassed. Our experiments show that using separate routing sub-vectors for the two MSTBs in each MSTG achieves similar ASSR performance. Thus, we share the same routing sub-vectors on the two MSTBs in each MSTG for model simplicity.

#### 3.3.1 Multi-Scale Transformer Block

By leveraging the power of multi-scale learning [29, 51, 52] and global learning [48, 39], we also propose a new Multi-Scale Transformer Block (MSTB) for comprehensive representation learning. Take the MSTB in the  $i$ -th MSTG as an example. As shown in Fig-

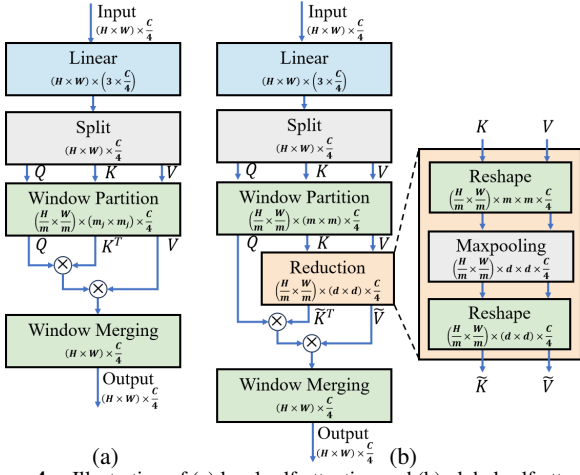


**Figure 4.** Illustration of (a) local self-attention and (b) global self-attention. In Figure 3 (b), the MSTB block in each MSTG mainly has three local self-attention (LSA) branches with different window sizes  $\{m_1, m_2, m_3\}$  to learn abundant multi-scale representation and a global self-attention (GSA) to provide global insight. It first splits the reshaped feature map  $F_{in} \in \mathbb{R}^{(H \times W) \times C}$  into four groups along the channel dimension, yielding  $\{F_j\}_{j=1}^4$  of size  $(H \times W) \times \frac{C}{4}$ . The routing sub-vector  $r^i$  indicates the forward path of four split feature maps  $\{F_j\}_{j=1}^4$ . If the routing value  $r_j^i = 1$ , the split feature map  $F_j$  will be fed into the  $j$ -th self-attention (LSA or GSA) branch. Otherwise if  $r_j^i = 0$ , the split feature map  $F_j$  will be set as a comfortable zero tensor and bypass the  $j$ -th attention branch. The outcome split feature  $O_j$  of this process can be expressed as:

$$O_j = \begin{cases} \text{SA}_j(F_j), & r_j^i = 1, \\ \mathbf{0}, & r_j^i = 0, \end{cases} \quad (1)$$

where  $\text{SA}_j$  is the  $j$ -th self-attention branch of this MSTB.

Subsequently, the outcome split features of four branches  $\{O_j\}_{j=1}^4$  are concatenated to obtain the outcome feature  $O_{cat}$ . The  $O_{cat}$  is further fed into our efficient slice-able linear projection. The resulting outcome feature  $O$  is then added to the input feature  $F_{in}$ , and further processed by a standard MLP in transformer blocks to output the feature  $F_{out}$  of this MSTB.

**Local self-attention (LSA).** As illustrated in Figure 4 (a), given an input feature of size  $(H \times W) \times \frac{C}{4}$ , the LSA branch first expands the channel dimension to  $\frac{3C}{4}$  by a linear layer and then splits it along the channel dimension into a Query matrix  $Q$ , a Key matrix  $K$ , and a Value matrix  $V$ , all of size  $(H \times W) \times \frac{C}{4}$ . The local window attention partitions  $Q, K, V$  into windows of size  $m_j \times m_j$  ( $j = 1, 2, 3$ ) and computes the attention map within each window. After performing self-attention along the window dimension, the LSA branch reshapes the attention feature  $\times \frac{C}{4}$  and output it for feature concatenation along the channel dimension.

**Global self-attention (GSA).** As shown in Figure 4 (b), our GSA branch is similar to the LSA branch on the first three steps of linear projection, feature split, and window partition. Since self-attention in large window size suffers from huge computational costs, we apply a dimension reduction on the Key matrix  $K$  and Value matrix  $V$  after the window partition step of our GSA branch, as suggested in [43, 44]. The window size of  $K$  and  $V$  is reduced from  $m \times m$  to  $d \times d$  ( $d < m$ ) by max-pooling, with proper reshape operations on the window dimensions. The dimension-reduced matrices  $\tilde{K}$  and  $\tilde{V}$  are used to perform self-attention with the Query matrix  $Q$ . Finally, the GSA branch reshapes the attention feature into  $(H \times W) \times \frac{C}{4}$  and output it for feature concatenation.

**Slice-able linear projection.** The output concatenated feature  $O_{cat}$

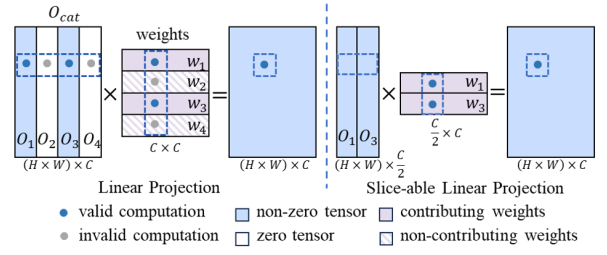


**Figure 5.** Illustration of our slice-able linear projection.

will be fused by linear projection in vanilla self-attention [34]. As shown in Figure 5, denoting  $W \in \mathbb{R}^{C \times C}$  as the weight matrix of linear projection, we split it along the row dimension and get four sub-matrices of  $W_1, W_2, W_3,$  and  $W_4$ , all of size  $\frac{C}{4} \times C$ . The vanilla linear projection is equivalent to multiplying the feature matrix  $O_j$  with the corresponding weight matrix  $W_j$  for  $j \in \{1, 2, 3, 4\}$ . In our MSTB, if the  $j$ -th branch is bypassed, its output split feature  $O_j \in \mathbb{R}^{(H \times W) \times C/4}$  will be a comfortable zero tensor, and the corresponding matrix multiplication in linear projection also outputs a zero tensor and hence can be bypassed.

To save possible computational costs, we design a slice-able linear projection by removing the zero tensors in the output feature  $O_{cat}$  and the corresponding sub-matrices in the weight matrix  $W$ . In our slice-able version, we multiply the outcome split feature  $O_j$  and the corresponding weight sub-matrix  $W_j$  with a routing value of  $r_j^i = 1$  for  $j = 1, 2, 3, 4$ , and denote them as  $O_j(r_j^i = 1)$  and  $W_j(r_j^i = 1)$ , respectively. Thus, the vanilla linear projection in our MSTB can be equally computed as

$$O_{cat} \times W = [O_j(r_j^i = 1)] \times [W_j^T(r_j^i = 1)]^T. \quad (2)$$

The proposed slice-able linear projection reduces the computational complexity of the vanilla linear projection from  $\mathcal{O}(HWC^2)$  to  $\mathcal{O}(\frac{1}{4} \sum_{j=1}^4 r_j^i HWC^2)$ . Figure 5 gives an example of  $r_2^i = r_4^i = 0$ , where  $O_{cat} \times W = [O_1, O_3] \times [W_1^T, W_3^T]^T$ .

### 3.3.2 Task-Aware Routing Controller

The goal of our Task-Aware Routing Controller (TARC) is to predict the inference path of the feature extraction backbone for each ASSR task, consisting of an LR image and an SR scale. As shown in Figure 3 (c), our TARC is a two-branch module to process the LR image and SR scale, respectively. The image branch estimates a sampling probability vector  $e \in \mathbb{R}^{4N}$  for the  $4N$  branches from the LR image, while the scale branch refines the probability vector by predicting an intensity scalar  $\beta$  to indicate the difficulty of ASSR on this SR scale.

For the image branch, we estimate the sampling probability vector  $e$  from the LR image  $I^{LR}$  through two  $3 \times 3$  convolutions followed by an average pooling and a linear projection. For  $i \in \{1, \dots, N\}$  and  $j \in \{1, 2, 3, 4\}$ , the element  $e_j^i$  of probability vector  $e$  is the probability of whether using the  $j$ -th self-attention branch of MSTBs in the  $i$ -th MSTG, estimated from the LR image  $I^{LR}$ . Therefore, the probability vector  $e$  varies for different LR images, which makes our TARC image-aware.

To further make our TARC module aware of SR scales (*i.e.*, scale-aware), its scale branch transforms the SR scale  $s$  to a scale-aware intensity scalar  $\beta$  via three linear layers, as shown in Figure 3 (c). Then the scale-aware intensity scalar  $\beta$  is used to refine the probability vector  $e$  to output the task-aware probability vector  $p$ :

$$p_j^i = \min \left( \beta \times 4N \times \sigma(e_j^i) / \sum_{i=1}^N \sum_{j=1}^4 \sigma(e_j^i), 1 \right), \quad (3)$$

where  $\sigma$  is the sigmoid function. We interpret  $\beta$  as the intensity of our TARC to modulate all the  $4N$  elements of the probability vector  $e$ . A small (or large)  $\beta$  implies that our TARC tends to decrease (or increase) the element values of the task-aware probability vector  $p$ .

With the scale-aware probability vector  $p$ , each element  $r_j^i \in \{0, 1\}$  ( $i \in \{1, \dots, N\}, j \in \{1, 2, 3, 4\}$ ) of the routing vector  $r$  can be drawn from Bernoulli sampling of  $p_j^i$ . Since Bernoulli sampling is a non-differentiable operation, the gradient of the loss function  $\mathcal{L}$  (will be introduced in §3.4) with respect to the routing value  $r_j^i$  cannot be computed in backward pass. To resolve this issue, as suggested in [55, 20, 23], we combine Straight-Through Estimator (STE) [3, 24] with the Bernoulli sampling to make our TARC trainable. The STE enables the backward pass of Bernoulli sampling to approximate the outgoing gradient by the incoming one. Thus, we formalize the forward and backward passes of STE as:

$$\begin{aligned} \text{STE Forward Pass: } r_j^i &\sim \text{Bernoulli}(p_j^i), \\ \text{STE Backward Pass: } \frac{\partial \mathcal{L}}{\partial r_j^i} &= \frac{\partial \mathcal{L}}{\partial p_j^i}. \end{aligned} \quad (4)$$

In this way, the Bernoulli sampling can be learnable by approximating the gradient  $\partial \mathcal{L} / \partial r_j^i$  by the gradient  $\partial \mathcal{L} / \partial p_j^i$ .

### 3.4 Loss Function

The loss function  $\mathcal{L}$  is a combination of the commonly used  $\mathcal{L}_1$  loss and our newly proposed penalty loss  $\mathcal{L}_\beta$  (which will be defined later) on the scale-aware intensity scalar  $\beta$ :

$$\mathcal{L} = \mathcal{L}_1 + \lambda \mathcal{L}_\beta, \quad (5)$$

where  $\lambda = 2 \times 10^{-4}$  is used to balance the two losses. Here, penalty loss  $\mathcal{L}_\beta$  is responsible to control scale-aware intensity  $\beta$  in Eqn. (3). Since the scale-aware scalar  $\beta$  implies the intensity of our TARC to select the  $4N$  self-attention branches, it should be penalized by a loss function to constraint the computational budget. A naive design is  $\mathcal{L}_\beta = \beta$ , but it potentially results in a small  $\beta$  for all scale factors. To avoid this problem, we simply incorporate a binary mask  $M \in \{0, 1\}$  on  $\beta$  in  $\lambda \mathcal{L}_\beta$ , and  $M$  is thresholded by the scale  $s$  as follows:

$$M \triangleq \beta \geq (\alpha_1 + \alpha_2 s^{\alpha_3}). \quad (6)$$

Then we can set the penalty loss  $\mathcal{L}_\beta$  of the scalar  $\beta$  by:

$$\mathcal{L}_\beta = \beta M. \quad (7)$$

We set  $\alpha_1 = 0.25$ ,  $\alpha_2 = 0.25$ , and  $\alpha_3 = 0.5$ .

## 4 Experiments

### 4.1 Experimental Setup

**Dataset.** Following previous ASSR works [9, 27, 50, 6], we use the training set of DIV2K [1] for model training. For model evaluation, we report Peak Signal-to-Noise Ratio (PSNR) results on the DIV2K validation set [1] and benchmark datasets, including B100 [36], Urban100 [22] and Manga109 [37].

**Implementation details.** We implement two variants of TADT feature extractor: 1) the Baseline, *i.e.*, the feature extraction backbone of our TADT (without the TARC), 2) the TADT. We combine our TADT variants with the arbitrary scale upsamplers of MetaSR [18], LIIF [9], or LTE [27] as our ASSR networks. All the three TADT variants comprise  $N = 8$  MSTGs with  $C = 224$  channels. Each MSTB in MSTGs has a global window size of  $m = 48$  and local window sizes

of  $\{m_1 = 4, m_2 = 8, m_3 = 16\}$ . Following [9], we set the channel dimension of the final output feature as  $C_{out} = 64$ .

For network training, we employ the same experimental setup of previous works [9, 27]. To synthesize paired HR and LR data, given the images from the DIV2K training set and an SR scale  $s$  evenly sampled from the uniform distribution  $\mathcal{U}(1, 4)$ , we first crop  $48s \times 48s$  patches from the images as the ground-truth (GT) HR images, and then utilize bicubic downsampling to get the paired LR images of size  $48 \times 48$ . We sample  $48 \times 48$  pixels from the same coordinates of the SR image and the GT HR images to compute the training loss.

We train our TADT variants with each arbitrary-scale upsampler, *i.e.*, MetaSR [18], LIIF [9], or LTE [27], as our ASSR networks described in §3.2. Note that our Baseline is scale-agnostic and thus trained with only the  $\mathcal{L}_1$  loss function by setting  $\lambda = 0$  in the loss function (5). Our TADT is trained on the pre-trained Baseline under the same settings, but with the loss function (5).

### 4.2 Main Results

**Quantitative results.** We compare our TADT variants with six off-the-shelf feature extractors, *i.e.*, EDSR-baseline [31], RDN [54], RCAN [53], NLSA [38], SwinIR [30], and CAT-R-2 [11]. The PSNR results on the DIV2K validation set and the five benchmark datasets are summarized in Table 1 and Table 10, respectively. We also provide results of other ASSR methods including ArbSR [42], LIRCAN [5] and EQSR [46] in Table 10 for reference. Our TADT achieves overall superior performance across all the test sets and SR scales, when working with MetaSR [18], LIIF [9], or LTE [27]. More results can be found in our supplementary materials.

**Qualitative results.** We provide the qualitative results of TADT along with comparison feature extractors in Figure 9. Here, we compare our TADT with NLSA [38], SwinIR [30], and CAT-R-2 [11], since they achieve comparable PSNR results in Tables 1 and 10. We observe that the SR results of different upsamplers working with our TADT exhibit more accurate structures, *e.g.*, the shape of character ‘‘S’’ (the 2-nd row) and the shape of X-type steel pole (the 3-rd row), as well as the textures of stone (the 1-st row), than the SR results of these upsamplers working with the other feature extractors.

**Computational costs.** In Table 3, we summarize the parameter amounts and computational costs of different feature extractors when working with the upsampler LIIF [9]. One can see that our Baseline and TADT are more efficient on both aspects than other competitors.

### 4.3 Ablation Study

Here, we perform ablation studies to investigate the working mechanism of our TADT feature extractor on image ASSR tasks. In all experiments, we use LIIF [9] as the arbitrary-scale upsampler to work with our TADT feature extractor.

**1) Does the scale branch in our TARC contribute to our TADT on scale-aware ASSR performance?** To answer this question, we compare our TADT with two other variants: a) directly using scale-agnostic  $\beta = 0.5$  and b) manually setting  $\beta = 0.25s$ , where  $s$  is the SR scale. As summarized in Table 6, although achieving reasonable results on  $\times 2$  upsampling, our ASSR network with  $\beta = 0.5$  in our TARC suffers from inferior PSNR results on upsampling for higher scales when compared with our TADT. Manually setting  $\beta = 0.25s$  enables our ASSR network to achieve comparable results with our TADT at high SR scales of  $s = 6, 8$ , but falls short in ASSR at lower scales, *e.g.*, 0.08 dB lower than our TADT on  $\times 2$  SR tasks. Our TADT well balances the performance across all the scales. As revealed in

**Table 1. Quantitative (PSNR (dB)) comparison of different feature extractors working with any arbitrary-scale upsampler on the DIV2K validation set.** † indicates our implementation, while the others are directly evaluated with the released pre-trained models. “-” indicates unavailable results due to out-of-memory (OOM) issue. The best results are highlighted in **bold**.

Method		In-scale			Out-of-scale				
Upsampler	Feature Extractor	×2	×3	×4	×6	×12	×18	×24	×30
MetaSR [18]	EDSR-baseline [31]	34.64	30.93	28.92	26.61	23.55	22.03	21.06	20.37
	RDN [54]	35.00	31.27	29.25	26.88	23.73	22.18	21.17	20.47
	RCAN† [53]	35.02	31.29	29.26	26.89	23.74	22.20	21.18	20.48
	NLSA† [38]	-	31.32	29.30	26.93	23.80	22.26	21.26	20.54
	SwinIR [30]	35.15	31.40	29.33	26.94	23.80	22.26	21.26	20.54
	CAT-R-2† [11]	35.15	31.38	29.29	26.90	23.77	22.23	21.24	20.52
	Baseline (Ours)	35.15	31.38	29.31	26.92	23.76	22.21	21.20	20.50
TADT (Ours)	<b>35.21</b>	<b>31.47</b>	<b>29.41</b>	<b>27.02</b>	<b>23.87</b>	<b>22.31</b>	<b>21.31</b>	<b>20.58</b>	
LIIF [9]	EDSR-baseline [31]	34.67	30.96	29.00	26.75	23.71	22.17	21.18	20.48
	RDN[54]	34.99	31.26	29.27	26.99	23.89	22.34	21.34	20.59
	RCAN† [53]	35.02	31.30	29.31	27.02	23.91	22.36	21.33	20.60
	NLSA† [38]	-	31.39	29.40	27.11	23.98	22.41	21.38	20.64
	SwinIR [30]	35.17	31.46	29.46	27.15	24.02	22.43	21.40	20.67
	CAT-R-2† [11]	35.23	31.49	29.49	27.18	24.03	22.45	21.41	20.67
	Baseline (Ours)	35.24	31.51	29.50	27.19	24.04	22.46	21.42	20.69
TADT (Ours)	<b>35.28</b>	<b>31.55</b>	<b>29.54</b>	<b>27.23</b>	<b>24.07</b>	<b>22.49</b>	<b>21.45</b>	<b>20.71</b>	
LTE [27]	EDSR-baseline [31]	34.72	31.02	29.04	26.81	23.78	22.23	21.24	20.53
	RDN [54]	35.04	31.32	29.33	27.04	23.95	22.40	21.36	20.64
	RCAN† [53]	35.02	31.30	29.31	27.04	23.95	22.40	21.38	20.65
	NLSA† [38]	-	31.44	29.44	27.14	24.03	22.48	21.44	20.70
	SwinIR [30]	35.24	31.50	29.51	27.20	24.09	22.50	21.47	20.73
	CAT-R-2† [11]	35.27	31.52	29.52	27.21	24.09	22.51	21.46	20.73
	Baseline (Ours)	35.27	31.53	29.52	27.21	24.08	22.50	21.46	20.73
TADT (Ours)	<b>35.31</b>	<b>31.56</b>	<b>29.56</b>	<b>27.24</b>	<b>24.10</b>	<b>22.52</b>	<b>21.48</b>	<b>20.75</b>	

**Table 2. Quantitative (PSNR (dB)) comparison of different ASSR methods on benchmark datasets.** † indicates our implementation, while the others are directly evaluated with the released pre-trained models. The best results are highlighted in **bold**.

Method		B100					Urban100					Manga109				
Upsampler	Feature Extractor	×2	×3	×4	×6	×8	×2	×3	×4	×6	×8	×2	×3	×4	×6	×8
MetaSR [18]	RDN [54]	32.33	29.26	27.71	25.90	24.83	32.92	28.82	26.55	23.99	22.59	-	-	-	-	-
	RCAN† [53]	32.35	29.29	27.73	25.91	24.83	33.14	28.98	26.66	24.06	22.65	39.37	34.44	31.26	26.97	24.5
	NLSA† [38]	32.35	29.30	27.77	25.95	24.88	33.25	29.12	26.80	24.20	22.78	39.43	34.55	31.42	27.11	24.71
	SwinIR [30]	32.39	29.31	27.75	25.94	24.87	33.29	29.12	26.76	24.16	22.75	39.42	34.58	31.34	26.96	24.62
	CAT-R-2† [11]	32.40	29.29	27.72	25.91	24.85	33.35	29.11	26.69	24.11	22.73	39.49	34.52	31.17	26.86	24.54
	Baseline (Ours)	32.40	29.32	27.74	25.92	24.85	33.34	29.12	26.74	24.14	22.74	39.47	34.53	31.28	26.88	24.53
	TADT (Ours)	<b>32.47</b>	<b>29.36</b>	<b>27.80</b>	<b>25.97</b>	<b>24.91</b>	<b>33.50</b>	<b>29.32</b>	<b>26.96</b>	<b>24.32</b>	<b>22.91</b>	<b>39.57</b>	<b>34.76</b>	<b>31.59</b>	<b>27.20</b>	<b>24.79</b>
LIIF [9]	RDN [54]	32.32	29.26	27.74	25.98	24.91	32.87	28.82	26.68	24.20	22.79	39.22	34.14	31.15	27.30	25.00
	RCAN† [53]	32.36	29.29	27.77	26.01	24.95	33.17	29.03	26.86	24.35	22.92	39.37	34.34	31.31	27.37	25.05
	NLSA† [38]	32.39	29.35	27.83	26.06	24.99	33.44	29.35	27.15	24.58	23.07	39.58	34.67	31.65	27.65	25.26
	SwinIR [30]	32.39	29.34	27.84	26.07	25.01	33.36	29.33	27.15	24.59	23.14	39.53	34.65	31.67	27.66	25.28
	CAT-R-2† [11]	32.44	29.38	27.86	26.09	25.02	33.58	29.44	27.23	24.67	23.19	39.53	34.66	31.69	27.72	25.31
	Baseline (Ours)	32.44	29.38	27.85	26.08	25.03	33.54	29.49	27.27	24.68	23.22	39.63	34.74	31.77	27.74	25.34
	TADT (Ours)	<b>32.46</b>	<b>29.41</b>	<b>27.87</b>	<b>26.10</b>	<b>25.05</b>	<b>33.65</b>	<b>29.58</b>	<b>27.37</b>	<b>24.75</b>	<b>23.27</b>	<b>39.68</b>	<b>34.79</b>	<b>31.83</b>	<b>27.84</b>	<b>25.39</b>
LTE [27]	RDN [54]	32.36	29.30	27.77	26.01	24.95	33.04	28.97	26.81	24.28	22.88	39.25	34.28	31.27	27.46	25.09
	RCAN† [53]	32.37	29.31	27.77	26.01	24.96	33.13	29.04	26.88	24.33	22.92	39.41	34.39	31.30	27.44	25.09
	NLSA† [38]	32.43	29.39	27.86	26.08	25.02	33.56	29.43	27.25	24.62	23.15	39.64	34.69	31.66	27.83	25.37
	SwinIR [30]	32.44	29.39	27.86	26.09	25.03	33.50	29.41	27.24	24.62	23.17	39.60	34.76	31.76	27.81	25.39
	CAT-R-2† [11]	32.47	29.39	27.87	26.09	25.03	33.60	29.48	27.27	24.68	23.21	39.61	34.75	31.76	27.84	25.39
	Baseline (Ours)	32.46	29.39	27.86	26.09	25.04	33.67	29.51	27.33	24.67	23.23	39.66	34.77	31.77	27.85	25.39
	TADT (Ours)	<b>32.47</b>	<b>29.41</b>	<b>27.88</b>	<b>26.11</b>	<b>25.05</b>	<b>33.70</b>	<b>29.57</b>	<b>27.36</b>	<b>24.72</b>	<b>23.26</b>	<b>39.72</b>	<b>34.86</b>	<b>31.85</b>	<b>27.93</b>	<b>25.47</b>
ArbSR (ICCV’2021) [42]	32.39	29.32	27.76	25.74	24.55	33.14	28.98	26.68	22.70	22.13	39.37	34.55	31.36	26.18	23.58	
LIRCAN (IJCAI’2023) [5]	32.42	29.36	27.82	-	-	33.13	29.11	26.88	-	-	39.56	34.77	31.71	-	-	
EQSR (CVPR’2023) [46]	32.46	<b>29.42</b>	27.86	26.07	-	33.62	29.53	27.30	24.66	-	39.44	<b>34.89</b>	<b>31.86</b>	<b>27.97</b>	-	

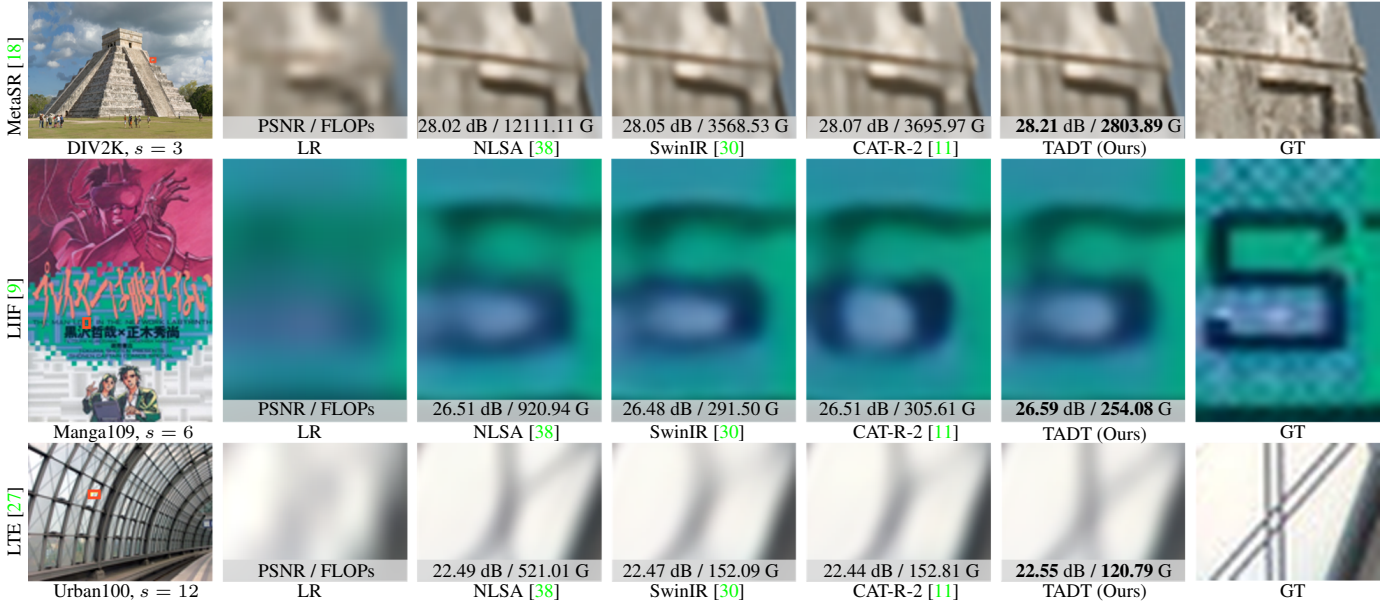


**Figure 6. Visual comparison of different ASSR networks for natural image ASSR.** The ASSR networks are made up of different feature extractors and arbitrary-scale upsamplers, *i.e.*, MetaSR [18] (1-st row), LIIF [9] (2-nd row), and LTE [27] (3-rd row). The highlighted regions are zoomed in for better view.

**Table 3. Parameter amounts (M) and FLOPs (G) of different feature extractors working with LIIF [9], for ASSR at scale  $s = 2$ , 3, or 4 on the DIV2K validation set.** “-”: the result is unavailable due to out-of-memory.

Feature Extractor	Params (M)	FLOPs (G)		
		$\times 2$	$\times 3$	$\times 4$
RDN [54]	21.97	15567.48	6918.88	3891.87
RCAN [53]	15.33	10774.88	4788.83	2693.72
SwinIR [30]	11.60	8832.28	3923.36	2227.08
NLSA [38]	39.58	-	13357.80	7513.77
CAT-R-2 [11]	11.63	8760.82	4038.19	2274.76
Baseline (Ours)	9.17	7454.65	3407.59	1952.41
TADT (Ours)	9.18	6986.92	3207.16	1845.57

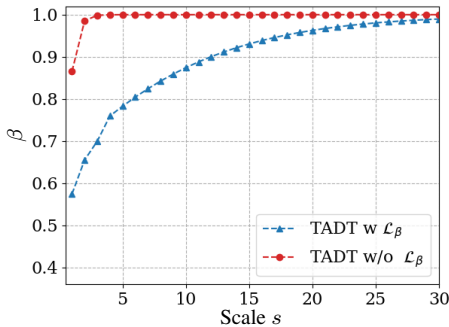


**Figure 7. The predicted  $\beta$  in our TADT w.r.t. different SR scales  $s$ .**

Figure 8  $\beta$  in our TADT basically grows with the SR scale in ASSR, which is consistent with our intent on its role of intensity indicator.

**2) The influence of penalty loss  $\mathcal{L}_\beta$  to our ASSR network.** We investigate this point by comparing our ASSR networks trained with or without using  $\mathcal{L}_\beta$ . In Figure 8, we visualize the curves of predicted  $\beta$  v.s. SR scales after training our TADT based ASSR network with  $\mathcal{L}_\beta$  and without  $\mathcal{L}_\beta$ . We observe that, without using  $\mathcal{L}_\beta$  in training, our ASSR networks are prone to predict saturated  $\beta$  when the SR scale increases, with higher computational costs. As summarized in Table 5, training our TADT without  $\mathcal{L}_\beta$  obtains a minor PSNR increase of 0.02dB for  $\times 2$  SR tasks on the DIV2K validation set, but also leads to a 388.75G FLOPs growth on computational costs. Therefore, it is necessary to use our intensity penalty loss  $\mathcal{L}_\beta$  in training our ASSR networks for computational efficiency.

**Table 4. PSNR (dB) results of our ASSR network with different designs of intensity indicator  $\beta$  on Urban100 [22].**

$\beta$	In-scale			Out-of-scale	
	$\times 2$	$\times 3$	$\times 4$	$\times 6$	$\times 8$
$\beta = 0.5$	33.66	29.53	27.33	24.72	23.23
$\beta = 0.25s$	33.57	29.53	27.34	24.74	23.24
Our TARC	33.65	29.58	27.37	24.75	23.27

**Table 5. Results of PSNR (dB) and FLOPs (G) by our TADT trained with (w) or without (w/o) the intensity loss  $\mathcal{L}_\beta$  on the DIV2K validation set.**

Feature Extractor	$\times 2$		$\times 3$		$\times 4$	
	PSNR	FLOPs	PSNR	FLOPs	PSNR	FLOPs
TADT, w $\mathcal{L}_\beta$	35.28	6986.91	31.55	3207.16	29.54	1845.57
TADT, w/o $\mathcal{L}_\beta$	35.30	7375.66	31.56	3378.02	29.55	1936.01

## 5 Conclusion

In this paper, we proposed an efficient feature extractor, *i.e.*, the Task-Aware Dynamic Transformer (TADT), for image ASSR. The proposed TADT contains cascaded multi-scale transformer groups (MSTGs) as the feature extraction backbone and a task-aware routing controller (TARC). Each MSTG group consists of two multi-scale transformer blocks (MSTBs). Each MSTB block has three local self-attention branches to learn useful multi-scale representations and a global self-attention branch to extract distant correlations. Given an inference task, *i.e.*, an input image and an SR scale, our TARC routing controller predicts the inference paths within the self-attention branches of our TADT backbone. With task-aware dynamic architecture, our TADT achieved efficient ASSR performance when compared to the mainstream feature extractors.

## Acknowledgements

This research is supported in part by The National Natural Science Foundation of China (No. 12226007 and 62176068) and the Open Research Fund from the Guangdong Provincial Key Laboratory of Big Data Computing, The Chinese University of Hong Kong, Shenzhen, under Grant No. B10120210117-OF03.

## References

- [1] E. Agustsson and R. Timofte. Ntire 2017 challenge on single image super-resolution: Dataset and study. In *CVPR Workshop*, July 2017.
- [2] S. Anwar, S. Khan, and N. Barnes. A deep journey into super-resolution: A survey. *ACM Computing Surveys*, 53(3), May 2020.
- [3] Y. Bengio, N. Léonard, and A. Courville. Estimating or propagating gradients through stochastic neurons for conditional computation. *arXiv preprint arXiv:1308.3432*, 2013.
- [4] J. Cao, Q. Wang, Y. Xian, Y. Li, B. Ni, Z. Pi, K. Zhang, Y. Zhang, R. Timofte, and L. Van Gool. Cioasr: Continuous implicit attention-in-attention network for arbitrary-scale image super-resolution. In *CVPR*, 2023.
- [5] J. Chao, Z. Zhou, H. Gao, J. Gong, Z. Zeng, and Z. Yang. A novel learnable interpolation approach for scale-arbitrary image super-resolution. In *IJCAI*, pages 564–572, 2023.
- [6] H.-W. Chen, Y.-S. Xu, M.-F. Hong, Y.-M. Tsai, H.-K. Kuo, and C.-Y. Lee. Cascaded local implicit transformer for arbitrary-scale super-resolution. In *CVPR*, pages 18257–18267, June 2023.
- [7] J. Chen, X. Wang, Z. Guo, X. Zhang, and J. Sun. Dynamic region-aware convolution. *CVPR*, pages 8060–8069, 2020.
- [8] L. Chen, H. Zhang, J. Xiao, L. Nie, J. Shao, W. Liu, and T.-S. Chua. Sca-cnn: Spatial and channel-wise attention in convolutional networks for image captioning. In *CVPR*, 2017.
- [9] Y. Chen, S. Liu, and X. Wang. Learning continuous image representation with local implicit image function. In *CVPR*, pages 8628–8638, 2021.
- [10] Z. Chen and H. Zhang. Learning implicit fields for generative shape modeling. In *CVPR*, pages 5939–5948, 2019.
- [11] Z. Chen, Y. Zhang, J. Gu, Y. Zhang, L. Kong, and X. Yuan. Cross aggregation transformer for image restoration. In *NeurIPS*, 2022.
- [12] J. Dai, H. Qi, Y. Xiong, Y. Li, G. Zhang, H. Hu, and Y. Wei. Deformable convolutional networks. In *ICCV*, pages 764–773, 2017.
- [13] C. Finn, P. Abbeel, and S. Levine. Model-agnostic meta-learning for fast adaptation of deep networks. In *ICML*, page 1126–1135, 2017.
- [14] S. Gao, X. Liu, B. Zeng, S. Xu, Y. Li, X. Luo, J. Liu, X. Zhen, and B. Zhang. Implicit diffusion models for continuous super-resolution. In *CVPR*, pages 10021–10030, June 2023.
- [15] A. Ghodrati, B. E. Bejnordi, and A. Habibian. Frameexit: Conditional early exiting for efficient video recognition. In *CVPR*, 2021.
- [16] D. Ha, A. M. Dai, and Q. V. Le. Hypernetworks. In *International Conference on Learning Representations*, 2017. URL <https://openreview.net/forum?id=rkpACe1lx>.
- [17] Y. Han, G. Huang, S. Song, L. Yang, H. Wang, and Y. Wang. Dynamic neural networks: A survey. *IEEE Transactions on Pattern Analysis and Machine Intelligence*, 44(11):7436–7456, 2021.
- [18] X. Hu, H. Mu, X. Zhang, Z. Wang, T. Tan, and J. Sun. Meta-sr: A magnification-arbitrary network for super-resolution. In *CVPR*, pages 1575–1584, 2019.
- [19] X. Hu, J. Xu, S. Gu, M.-M. Cheng, and L. Liu. Restore globally, refine locally: A mask-guided scheme to accelerate super-resolution networks. In *ECCV*, pages 74–91. Springer, 2022.
- [20] X. Hu, Z. Huang, A. Huang, J. Xu, and S. Zhou. A dynamic multi-scale voxel flow network for video prediction. In *CVPR*, pages 6121–6131, 2023.
- [21] G. Huang, D. Chen, T. Li, F. Wu, L. Van Der Maaten, and K. Q. Weinberger. Multi-scale dense networks for resource efficient image classification. *arXiv preprint arXiv:1703.09844*, 2017.
- [22] J.-B. Huang, A. Singh, and N. Ahuja. Single image super-resolution from transformed self-exemplars. In *CVPR*, pages 5197–5206, 2015.
- [23] Z. Huang, A. Huang, X. Hu, C. Hu, J. Xu, and S. Zhou. Scale-adaptive feature aggregation for efficient space-time video super-resolution. In *WACV*, 2024.
- [24] I. Hubara, M. Courbariaux, D. Soudry, R. El-Yaniv, and Y. Bengio. Quantized neural networks: Training neural networks with low precision weights and activations. *The Journal of Machine Learning Research*, 18(1):6869–6898, 2017.
- [25] Z. Jiang, C. Li, X. Chang, L. Chen, J. Zhu, and Y. Yang. Dynamic slimmable denoising network. *IEEE Transactions on Image Processing*, 32:1583–1598, 2023.
- [26] X. Kong, H. Zhao, Y. Qiao, and C. Dong. Classsr: A general framework to accelerate super-resolution networks by data characteristic. In *CVPR*, pages 12016–12025, June 2021.
- [27] J. Lee and K. H. Jin. Local texture estimator for implicit representation function. In *CVPR*, pages 1929–1938, June 2022.
- [28] C. Li, G. Wang, B. Wang, X. Liang, Z. Li, and X. Chang. Dynamic slimmable network. In *CVPR*, pages 8603–8613, 2021.
- [29] J. Li, F. Fang, K. Mei, and G. Zhang. Multi-scale residual network for image super-resolution. In *ECCV*, September 2018.
- [30] J. Liang, J. Cao, G. Sun, K. Zhang, L. Van Gool, and R. Timofte. Swinir: Image restoration using swin transformer. In *ICCV*, pages 1833–1844, 2021.
- [31] B. Lim, S. Son, H. Kim, S. Nah, and K. M. Lee. Enhanced Deep Residual Networks for Single Image Super-Resolution. *arXiv e-prints*, art. arXiv:1707.02921, July 2017.
- [32] J. Lin, Y. Rao, J. Lu, and J. Zhou. Runtime neural pruning. In I. Guyon, U. V. Luxburg, S. Bengio, H. Wallach, R. Fergus, S. Vishwanathan, and R. Garnett, editors, *NeurIPS*, volume 30, 2017.
- [33] L. Liu and J. Deng. Dynamic deep neural networks: Optimizing accuracy-efficiency trade-offs by selective execution. *ArXiv*, abs/1701.00299, 2017.
- [34] Z. Liu, Y. Lin, Y. Cao, H. Hu, Y. Wei, Z. Zhang, S. Lin, and B. Guo. Swin Transformer: Hierarchical Vision Transformer using Shifted Windows. *arXiv e-prints*, art. arXiv:2103.14030, Mar. 2021.
- [35] N. Ma, X. Zhang, J. Huang, and J. Sun. Weightnet: Revisiting the design space of weight networks. In *ECCV*, 2020.
- [36] D. Martin, C. Fowlkes, D. Tal, and J. Malik. A database of human segmented natural images and its application to evaluating segmentation algorithms and measuring ecological statistics. In *ICCV*, volume 2, pages 416–423 vol.2, 2001.
- [37] Y. Matsui, K. Ito, Y. Aramaki, A. Fujimoto, T. Ogawa, T. Yamasaki, and K. Aizawa. Sketch-based manga retrieval using manga109 dataset. *Multimedia Tools and Applications*, 76(20):21811–21838, 2017.
- [38] Y. Mei, Y. Fan, and Y. Zhou. Image super-resolution with non-local sparse attention. In *CVPR*, pages 3517–3526, June 2021.
- [39] Z. Tu, H. Talebi, H. Zhang, F. Yang, P. Milanfar, A. Bovik, and Y. Li. Maxvit: Multi-axis vision transformer. *ECCV*, 2022.
- [40] A. Vaswani, N. Shazeer, N. Parmar, J. Uszkoreit, L. Jones, A. N. Gomez, L. u. Kaiser, and I. Polosukhin. Attention is all you need. In *NeurIPS*, volume 30, 2017.
- [41] G. Vaudeaux-Ruth, A. Chan-Hon-Tong, and C. Achard. Actionspotter: Deep reinforcement learning framework for temporal action spotting in videos. In *ICPR*, pages 631–638, 2021.
- [42] L. Wang, Y. Wang, Z. Lin, J. Yang, W. An, and Y. Guo. Learning a single network for scale-arbitrary super-resolution. In *ICCV*, pages 4801–4810, 2021.
- [43] S. Wang, B. Z. Li, M. Khabisa, H. Fang, and H. Ma. Linformer: Self-Attention with Linear Complexity. *arXiv e-prints*, art. arXiv:2006.04768, June 2020.
- [44] W. Wang, E. Xie, X. Li, D.-P. Fan, K. Song, D. Liang, T. Lu, P. Luo, and L. Shao. Pyramid vision transformer: A versatile backbone for dense prediction without convolutions. In *ICCV*, pages 568–578, 2021.
- [45] X. Wang, F. Yu, Z.-Y. Dou, T. Darrell, and J. E. Gonzalez. SkipNet: Learning Dynamic Routing in Convolutional Networks. *arXiv e-prints*, art. arXiv:1711.09485, Nov. 2017.
- [46] X. Wang, X. Chen, B. Ni, H. Wang, Z. Tong, and Y. Liu. Deep arbitrary-scale image super-resolution via scale-equivariance pursuit. In *CVPR*, pages 1786–1795, 2023.
- [47] Z. Wu, C. Xiong, Y.-G. Jiang, and L. S. Davis. Liteeval: A coarse-to-fine framework for resource efficient video recognition. In *NeurIPS*, volume 32, 2019.
- [48] E. Xie, W. Wang, Z. Yu, A. Anandkumar, J. M. Alvarez, and P. Luo. Segformer: Simple and efficient design for semantic segmentation with transformers. In *NeurIPS*, 2021.
- [49] X. Xu, Z. Wang, and H. Shi. Ultrasr: Spatial encoding is a missing key for implicit image function-based arbitrary-scale super-resolution. *CoRR*, abs/2103.12716, 2021.
- [50] J. Yang, S. Shen, H. Yue, and K. Li. Implicit transformer network for screen content image continuous super-resolution. In A. Beygelzimer, Y. Dauphin, P. Liang, and J. W. Vaughan, editors, *NeurIPS*, 2021.
- [51] S. W. Zamir, A. Arora, S. Khan, M. Hayat, F. S. Khan, and M.-H. Yang. Restormer: Efficient transformer for high-resolution image restoration. In *CVPR*, 2022.
- [52] X. Zhang, H. Zeng, S. Guo, and L. Zhang. Efficient long-range attention network for image super-resolution. In *ECCV*, pages 649–667. Springer, 2022.
- [53] Y. Zhang, K. Li, K. Li, L. Wang, B. Zhong, and Y. Fu. Image super-resolution using very deep residual channel attention networks. In *ECCV*, pages 286–301, 2018.
- [54] Y. Zhang, Y. Tian, Y. Kong, B. Zhong, and Y. Fu. Residual dense network for image super-resolution. In *CVPR*, pages 2472–2481, 2018.
- [55] S. Zhou, Y. Wu, Z. Ni, X. Zhou, H. Wen, and Y. Zou. Dorefa-net: Training low bandwidth convolutional neural networks with low bandwidth gradients. *CoRR*, abs/1606.06160, 2016.
- [56] Y. Zhou, T. Ren, C. Zhu, X. Sun, J. Liu, X. Ding, M. Xu, and R. Ji. Trar: Routing the attention spans in transformer for visual question answering. In *ICCV*, pages 2054–2064, 2021.

## A Content

In this supplementary file, we further elaborate our Task-Aware Dynamic Transformer (TADT) as an efficient feature extractor for Arbitrary-Scale Image Super-Resolution. Specifically, we present

- more ablation studies of our TADT in Sec:ablation;
- more quantitative results of our TADT in appendix C;
- more visual comparisons of our TADT and other feature extractors on natural image ASSR in appendix D.

## B Ablation Studies

Here, we perform more ablation studies to investigate the working mechanism of our TADT feature extractor on image ASSR. Similar to the main paper, all ablation experiments here are conducted on our TADT integrated with the arbitrary-scale upsampler LIIF [9].

**1) Effectiveness of using binary mask  $M$  in our intensity loss  $\mathcal{L}_\beta$ .** To illustrate this point, we remove the binary mask  $M$  in  $\mathcal{L}_\beta$  and directly set  $\mathcal{L}_\beta = \beta$  in the loss function  $\mathcal{L}$  to train our TADT. We visualize the  $\beta$  with different  $s$  in our TADT when  $\mathcal{L}_\beta = \beta$  by the red curve in Figure 8. One can see that, the  $\beta$  value in our TADT goes a slight ascent and then sweep down to about 0.1, which is unreasonable. Quantitative results reported in Table 6 further demonstrate that excluding the mask  $M$  from the intensity loss  $\mathcal{L}_\beta$  leads to a significant performance drop, with a decrease of 0.09 dB for  $\times 8$  upsampling. This validates the effectiveness of using a binary mask  $M$  in our intensity loss  $\mathcal{L}_\beta$  to train our TADT for image ASSR.

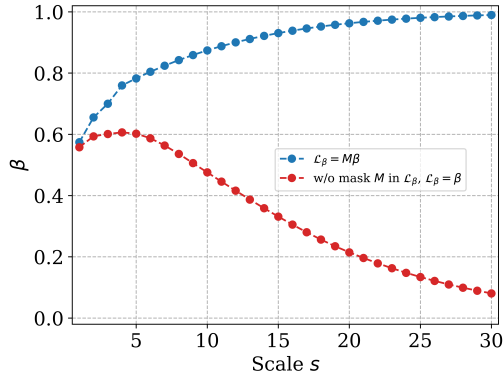


Figure 8. The predicted  $\beta$  in our TADT *w.r.t.* different SR scales  $s$ .

Table 6. PSNR (dB) results of our TADT trained with  $\mathcal{L}_\beta$  using the binary mask or not on Urban100 [22].

$\mathcal{L}_\beta$	In-scale			Out-of-scale	
	$\times 2$	$\times 3$	$\times 4$	$\times 6$	$\times 8$
$\mathcal{L}_\beta = \beta$	33.66	29.56	27.36	24.73	23.18
$\mathcal{L}_\beta = \beta M$	33.65	29.58	27.37	24.75	23.27

**2) Importance of the global self-attention (GSA) branch in the MSTB of our feature extraction backbone.** To study this aspect, we conduct experiments by evaluating our ASSR network with or without the GSA branch in each MSTB of our feature extraction backbone. Here, we use the Baseline instead of our TADT to use the complete feature extraction backbone for fully comparison. As shown in Table 7, our ASSR network using the Baseline with GSA achieves a performance gain of 0.06 dB on PSNR over that without GSA, on the DIV2K validation set for  $\times 2$  SR. This validates the importance of GSA branch in our feature extraction backbone for image ASSR.

**3) Investigation on dimension reduction in the GSA branch.** To this end, we explore other dimension reduction variants, *e.g.*, “Random Matrix” and “Avgpooling” for the GSA branch in our Baseline

Table 7. PSNR (dB) results of our Baseline with (w) or without (w/o) global self-attention (GSA) branch on the DIV2K validation set.

Extractor	In-scale			Out-of-scale	
	$\times 2$	$\times 3$	$\times 4$	$\times 6$	$\times 12$
w GSA	35.24	31.51	29.50	27.19	24.04
w/o GSA	35.18	31.45	29.45	27.14	24.02

Table 8. PSNR (dB) results of different dimension-reduction operations in global self-attention on DIV2K validation set.

Dimension Reduction	In-scale			Out-of-scale	
	$\times 2$	$\times 3$	$\times 4$	$\times 6$	$\times 12$
Random Matrix	35.22	31.48	29.49	27.16	24.00
Avgpooling	35.23	31.49	29.49	27.18	24.04
Maxpooling	35.24	31.51	29.50	27.19	24.04

Table 9. PSNR (dB) results of different hyper-parameter settings on Urban100.

Hyper-parameters	In-scale			Out-of-scale	
	$\times 2$	$\times 3$	$\times 4$	$\times 6$	$\times 8$
$\alpha_1 = 0.25, \alpha_2 = 0.25, \alpha_3 = 0.50$	33.65	29.58	27.37	24.75	23.27
$\alpha_1 = 0.00, \alpha_2 = 0.25, \alpha_3 = 1.00$	33.62	29.57	27.37	24.77	23.27
$\alpha_1 = 0.00, \alpha_2 = 0.25, \alpha_3 = 0.50$	33.64	29.52	27.32	24.61	23.02
$\alpha_1 = 0.25, \alpha_2 = 0.50, \alpha_3 = 0.50$	33.64	29.56	27.36	24.74	23.25

variant. Here, “Random Matrix” performs dimension reduction by a linear projection matrix of size  $m^2 \times d^2$ , which is randomly sampled from a normal distribution. For “Avgpooling”, we just replaces the “maxpooling” operation in the GSA by average pooling. As shown in Table 8, the “Maxpooling” employed in GSA achieves slightly better results (0.01~0.04dB) on ASSR tasks at most scales. Thus, we use “Maxpooling” for dimension reduction in the GSA branch.

**4) Investigation on the sensitivity of hyper-parameters.** In Eqn 6, we use  $\alpha_1, \alpha_2$  and  $\alpha_3$  to penalize the predicted  $\beta$  by a loss  $\mathcal{L}_\beta = \beta M$ , using a binary value  $M \triangleq \beta \geq (\alpha_1 + \alpha_2 s^{\alpha_3})$  to avoid small  $\beta$  values.  $\alpha_1$  is the lower bound of  $\beta$  to be penalized.  $\alpha_2$  and  $\alpha_3$  should be properly set to adjust the binary value  $M$  according to the scale  $s$ . We report the experimental results achieved by different hyper-parameter settings on Urban100 in Table 9. We observe that our TADT is not very sensitive to the values of  $\alpha_1, \alpha_2$  and  $\alpha_3$  once they are properly set, but our setting reported in paper achieves an overall better performance.

## C More Quantitative Results

In Table 10, we provide more quantitative results on Set5, Set14, B100, Urban100, and Manga109.

## D More Visual Comparison on Image ASSR

In Figures 9-14, we provide more visual comparison results of different feature extractors working with three arbitrary-scale upsamplers, *i.e.*, MetaSR [18], LIIF [9], and LTE [27], on the image ASSR task.

**Table 10. Quantitative comparison of PSNR (dB) results by different feature extractors working with arbitrary-scale upsamplers on five benchmark datasets.** † indicates our implementation, while the others are directly evaluated with the released pre-trained models. The best results are highlighted in **bold**.

Method		Set5			Set14			B100			Urban100			Manga109		
Upsampler	Feature Extractor	×2	×3	×4	×2	×3	×4	×2	×3	×4	×2	×3	×4	×2	×3	×4
MetaSR [18]	RDN [54]	38.22	34.63	32.38	33.98	30.54	28.78	32.33	29.26	27.71	32.92	28.82	26.55	-	-	-
	RCAN† [53]	38.24	34.69	32.44	34.02	30.59	28.81	32.35	29.29	27.73	33.14	28.98	26.66	39.37	34.44	31.26
	NLSA† [38]	38.26	34.76	32.51	34.11	30.68	28.89	32.35	29.30	27.77	33.25	29.12	26.80	39.43	34.55	31.42
	SwinIR [30]	38.26	34.77	32.47	34.14	30.66	28.85	32.39	29.31	27.75	33.29	29.12	26.76	39.42	34.58	31.34
	CAT-R-2† [11]	38.30	34.74	32.40	<b>34.21</b>	30.68	28.83	32.40	29.29	27.72	33.35	29.11	26.69	39.49	34.52	31.17
	Baseline (Ours)	TADT (Ours)	38.29	34.77	32.49	34.11	30.68	28.84	32.40	29.32	27.74	33.34	29.12	26.74	39.47	34.53
LIIF [9]	RDN [54]	38.17	34.68	32.50	33.97	30.53	28.80	32.32	29.26	27.74	32.87	28.82	26.68	39.22	34.14	31.15
	RCAN† [53]	38.21	34.74	32.59	34.02	30.61	28.89	32.36	29.29	27.77	33.17	29.03	26.86	39.37	34.34	31.31
	NLSA† [38]	38.30	34.86	32.73	34.22	30.72	28.98	32.39	29.35	27.83	33.44	29.35	27.15	39.58	34.67	31.65
	SwinIR [30]	38.28	34.87	32.73	34.14	30.75	28.98	32.39	29.34	27.84	33.36	29.33	27.15	39.53	34.65	31.67
	CAT-R-2† [11]	38.33	34.91	32.75	34.27	30.79	29.02	32.44	29.38	27.86	33.58	29.44	27.23	39.53	34.66	31.69
	Baseline (Ours)	TADT (Ours)	38.34	34.91	32.78	34.19	30.81	29.03	32.44	29.38	27.85	33.54	29.49	27.27	39.63	34.74
LTE [27]	RDN [54]	38.23	34.72	32.61	34.09	30.58	28.88	32.36	29.30	27.77	33.04	28.97	26.81	39.25	34.28	31.27
	RCAN† [53]	38.24	34.77	32.60	34.04	30.64	28.87	32.37	29.31	27.77	33.13	29.04	26.88	39.41	34.39	31.30
	NLSA† [38]	38.35	34.88	32.81	34.28	30.78	29.01	32.43	29.39	27.86	33.56	29.43	27.25	39.64	34.69	31.66
	SwinIR [30]	38.33	34.89	32.81	34.25	30.80	29.06	32.44	29.39	27.86	33.50	29.41	27.24	39.60	34.76	31.76
	CAT-R-2† [11]	38.36	34.91	32.80	34.24	30.81	29.04	32.47	29.39	27.87	33.60	29.48	27.27	39.61	34.75	31.76
	Baseline (Ours)	TADT (Ours)	38.39	34.95	<b>32.84</b>	34.25	30.80	<b>29.06</b>	32.46	29.39	27.86	33.67	29.51	27.33	39.66	34.77
ArbSR [42]	LIRCAN [5]	38.26	34.76	32.55	34.09	30.64	28.87	32.39	29.32	27.76	33.14	28.98	26.68	39.27	34.55	31.36
	EQSR [46]	38.29	34.82	32.68	34.33	30.77	28.97	32.42	29.36	27.82	33.13	29.11	26.88	39.56	34.77	31.71
	EQSR [46]	38.35	34.83	32.71	34.45	30.82	29.12	32.46	29.42	27.86	33.62	29.53	27.30	39.44	34.89	31.86
Upsampler	Feature Extractor	×6	×8	×12	×6	×8	×12	×6	×8	×12	×6	×8	×12	×6	×8	×12
MetaSR [18]	RDN [54]	29.04	26.96	-	26.51	24.97	-	25.90	24.83	-	23.99	22.59	-	-	-	-
	RCAN† [53]	29.02	26.97	24.63	26.55	25.01	23.20	25.91	24.83	23.47	24.06	22.65	21.05	26.97	24.57	22.01
	NLSA† [38]	29.07	27.00	24.72	26.56	25.07	23.25	25.95	24.88	23.51	24.20	22.78	21.15	27.11	24.71	22.13
	SwinIR [30]	29.09	27.02	24.66	26.58	25.09	23.23	25.94	24.87	23.52	24.16	22.75	21.16	26.96	24.62	22.10
	CAT-R-2† [11]	28.98	26.96	24.59	26.52	25.03	23.19	25.91	24.85	23.48	24.11	22.73	21.12	26.86	24.54	22.06
	Baseline (Ours)	TADT (Ours)	29.08	27.01	24.71	26.56	25.07	23.26	25.92	24.85	23.50	24.14	22.74	21.12	26.88	24.53
LIIF [9]	RDN [54]	29.15	27.14	24.86	26.64	25.15	23.24	25.98	24.91	23.57	24.20	22.79	21.15	27.30	25.00	22.36
	RCAN† [53]	29.32	27.27	24.81	26.69	25.23	23.29	26.01	24.95	23.59	24.35	22.92	21.24	27.37	25.05	22.39
	NLSA† [38]	29.39	27.24	24.90	26.73	25.26	23.34	26.06	24.99	23.62	24.58	23.07	21.39	27.65	25.26	22.53
	SwinIR [30]	29.46	27.36	24.98	26.82	25.34	23.37	26.07	25.01	23.64	24.59	23.14	21.43	27.66	25.28	22.57
	CAT-R-2† [11]	<b>29.53</b>	<b>27.38</b>	24.98	26.82	25.36	23.37	26.09	25.02	23.62	24.67	23.19	21.47	27.72	25.31	22.58
	Baseline (Ours)	TADT (Ours)	29.45	27.34	<b>25.03</b>	26.80	25.34	23.37	26.08	25.03	23.64	24.68	23.22	21.51	27.74	25.34
LTE [27]	RDN [54]	29.32	27.26	24.79	26.71	25.16	23.31	26.01	24.95	23.60	24.28	22.88	21.22	27.46	25.09	22.43
	RCAN† [53]	29.29	27.30	24.91	26.72	25.25	23.34	26.01	24.96	23.62	24.33	22.92	21.29	27.44	25.09	22.43
	NLSA† [38]	29.43	27.33	25.02	26.79	25.32	22.36	26.08	25.02	23.65	24.62	23.15	21.47	27.83	25.37	22.61
	SwinIR [30]	29.50	27.35	25.07	26.86	25.42	<b>23.44</b>	26.09	25.03	23.67	24.62	23.17	21.51	27.81	25.39	22.65
	CAT-R-2† [11]	29.41	27.33	24.96	26.85	25.34	23.40	26.09	25.03	23.65	24.68	23.21	21.50	27.84	25.39	22.66
	Baseline (Ours)	TADT (Ours)	29.46	27.39	25.04	<b>26.86</b>	<b>25.36</b>	23.41	26.09	25.04	23.66	24.67	23.23	21.51	27.85	25.39
ArbSR [42]	EQSR [46]	28.45	26.21	23.69	26.22	24.55	22.55	25.74	24.55	23.07	23.70	22.13	20.40	26.18	23.58	21.05
	EQSR [46]	29.41	-	-	26.79	-	-	26.07	-	-	24.66	-	-	27.97	-	-

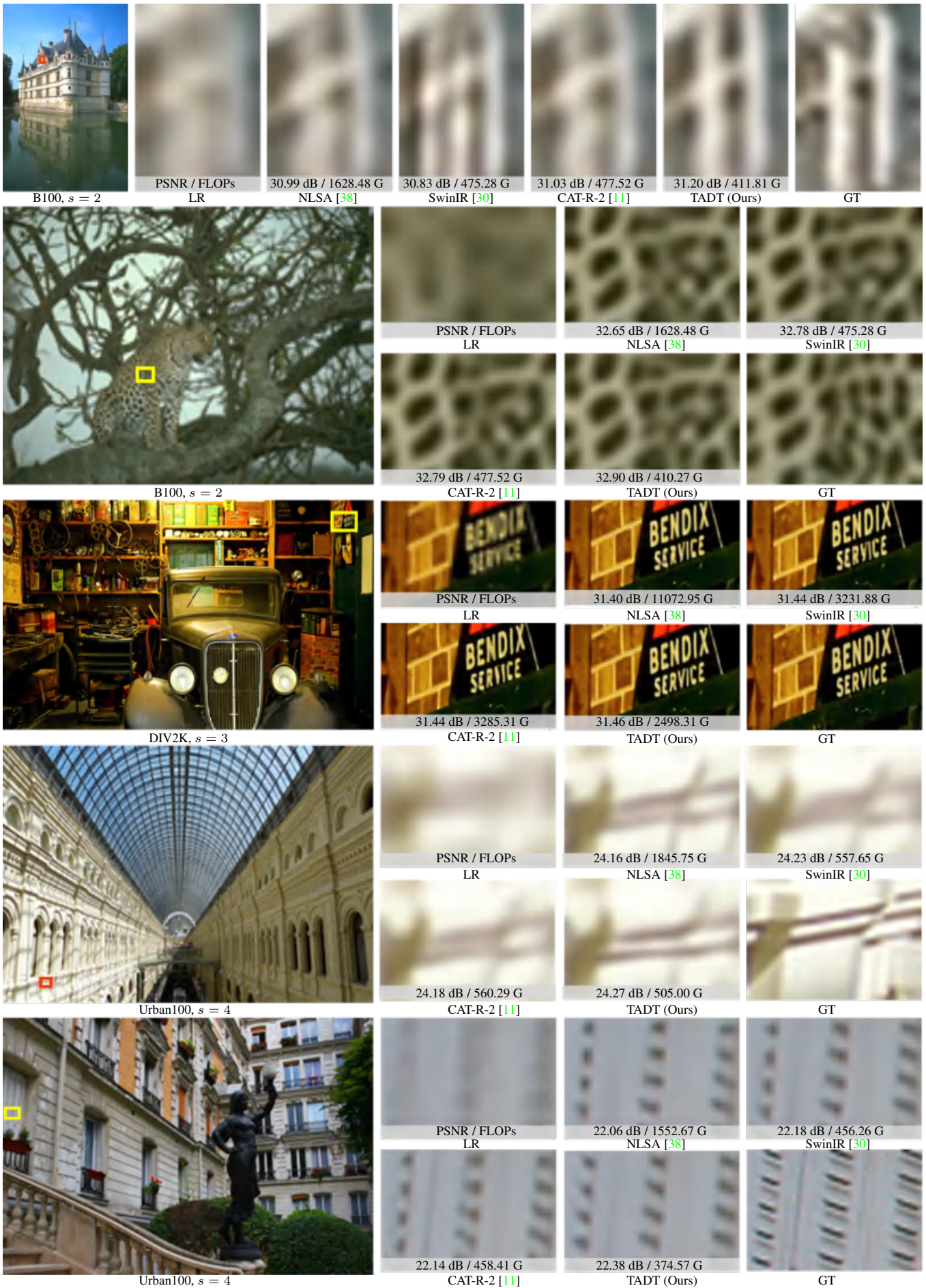


Figure 9. Visual comparison of feature extractors integrated with MetaSR [18] on super-resolution natural images at scale 2, 3, 4. The highlighted regions are zoomed in for better view.

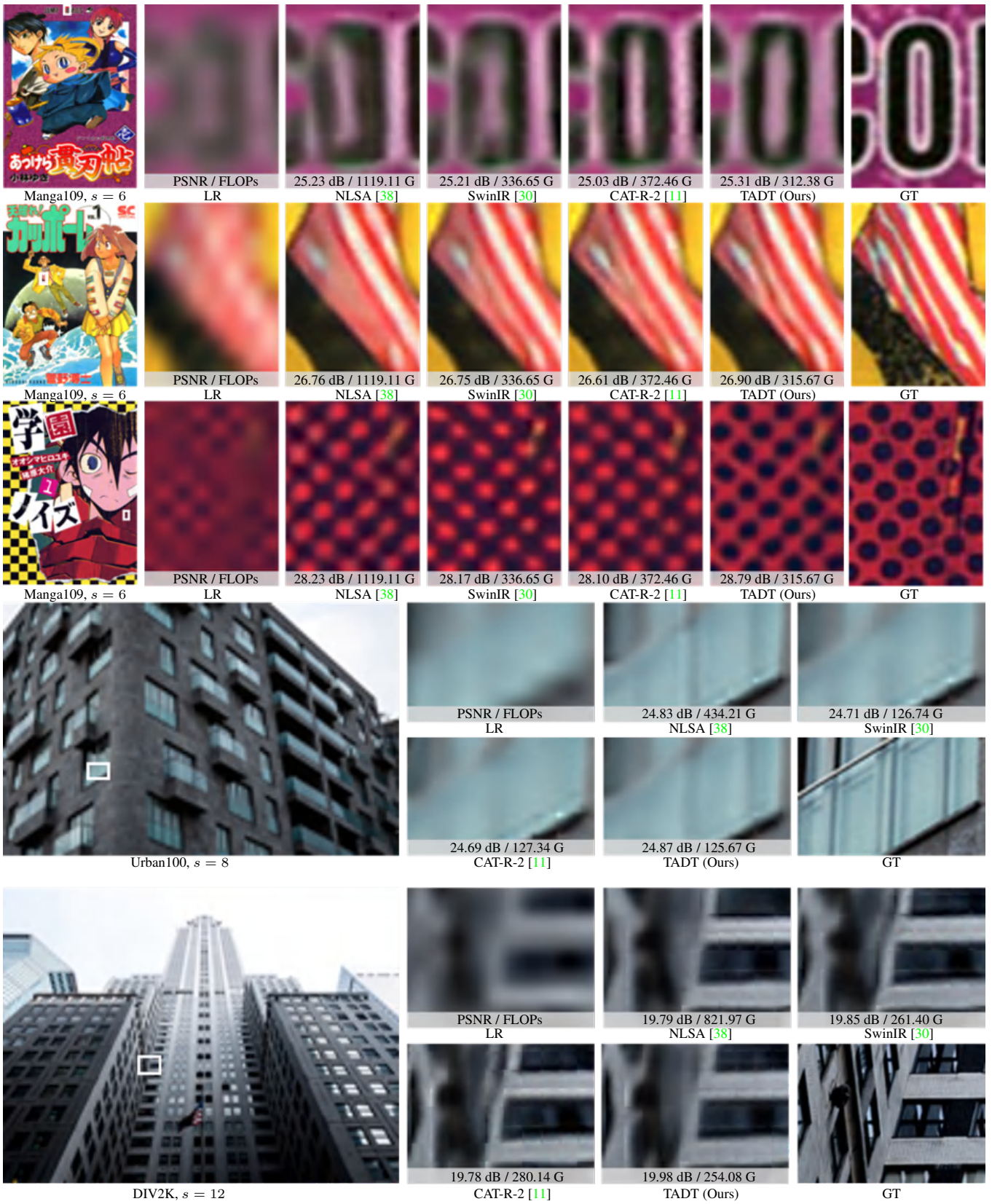


Figure 10. Visual comparison of feature extractors integrated with MetaSR [18] on super-resolution natural images at scale 6, 8, 12. The highlighted regions are zoomed in for better view.

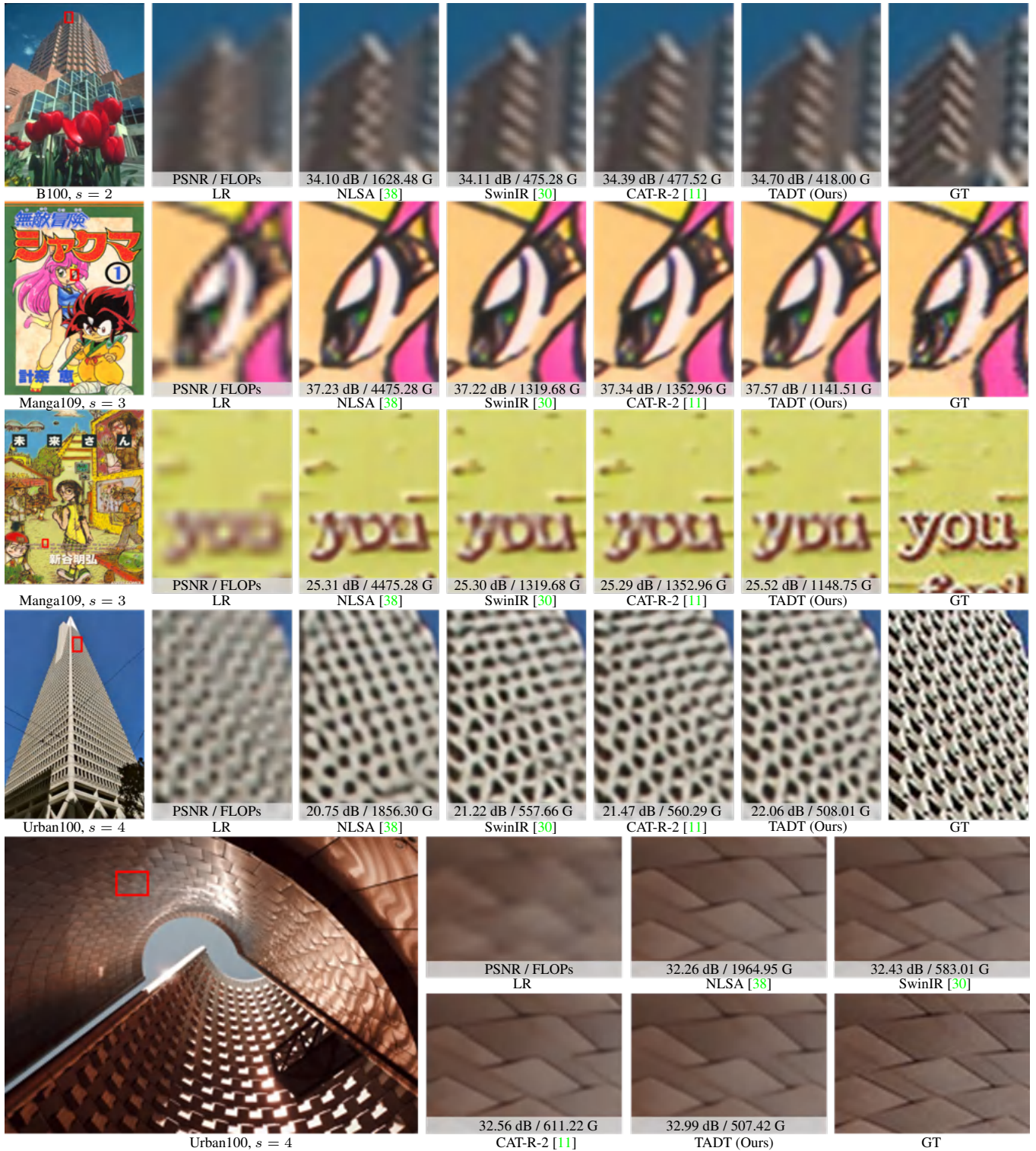


Figure 11. Visual comparison of feature extractors integrated with LIIF [9] on super-resolution for natural images at scale 2, 3, 4. The highlighted regions are zoomed in for better view.

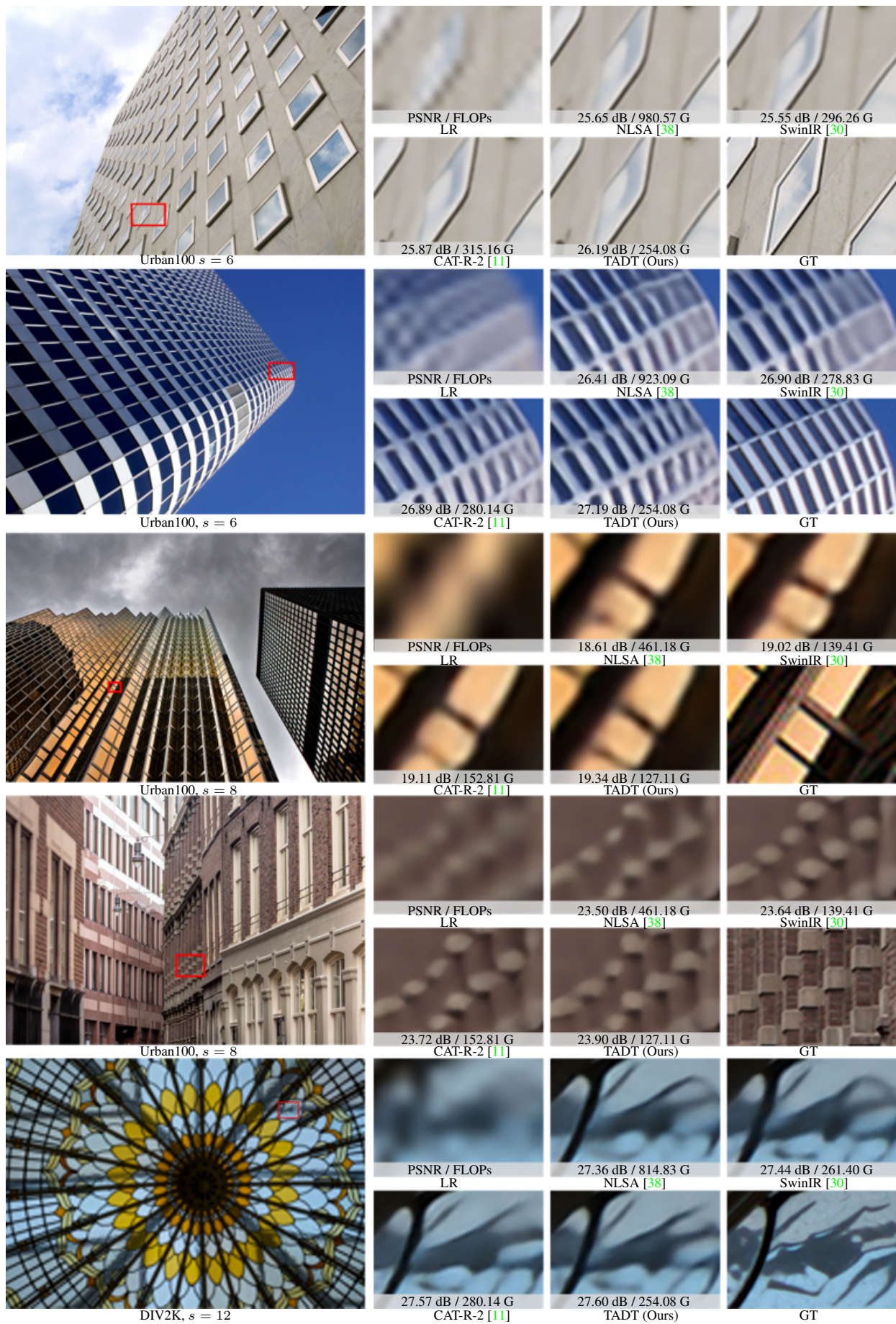


Figure 12. Visual comparison of feature extractors integrated with LIIF [9] on super-resolution for natural images at scale 6, 8, 12. The highlighted regions are zoomed in for better view.

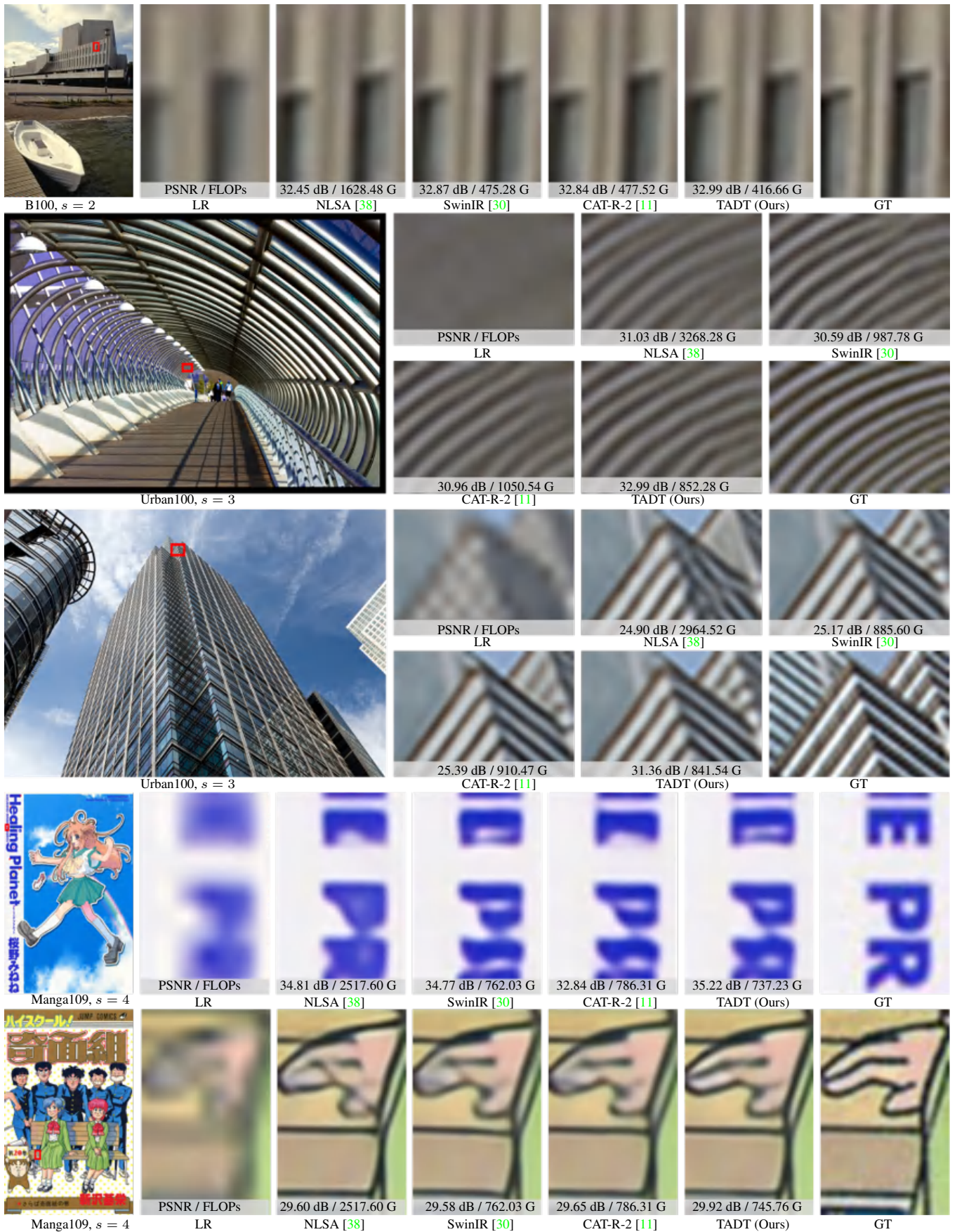


Figure 13. Visual comparison of feature extractors integrated with LTE [27] on super-resolution for natural images at scale 2, 3, 4. The highlighted regions are zoomed in for better view.

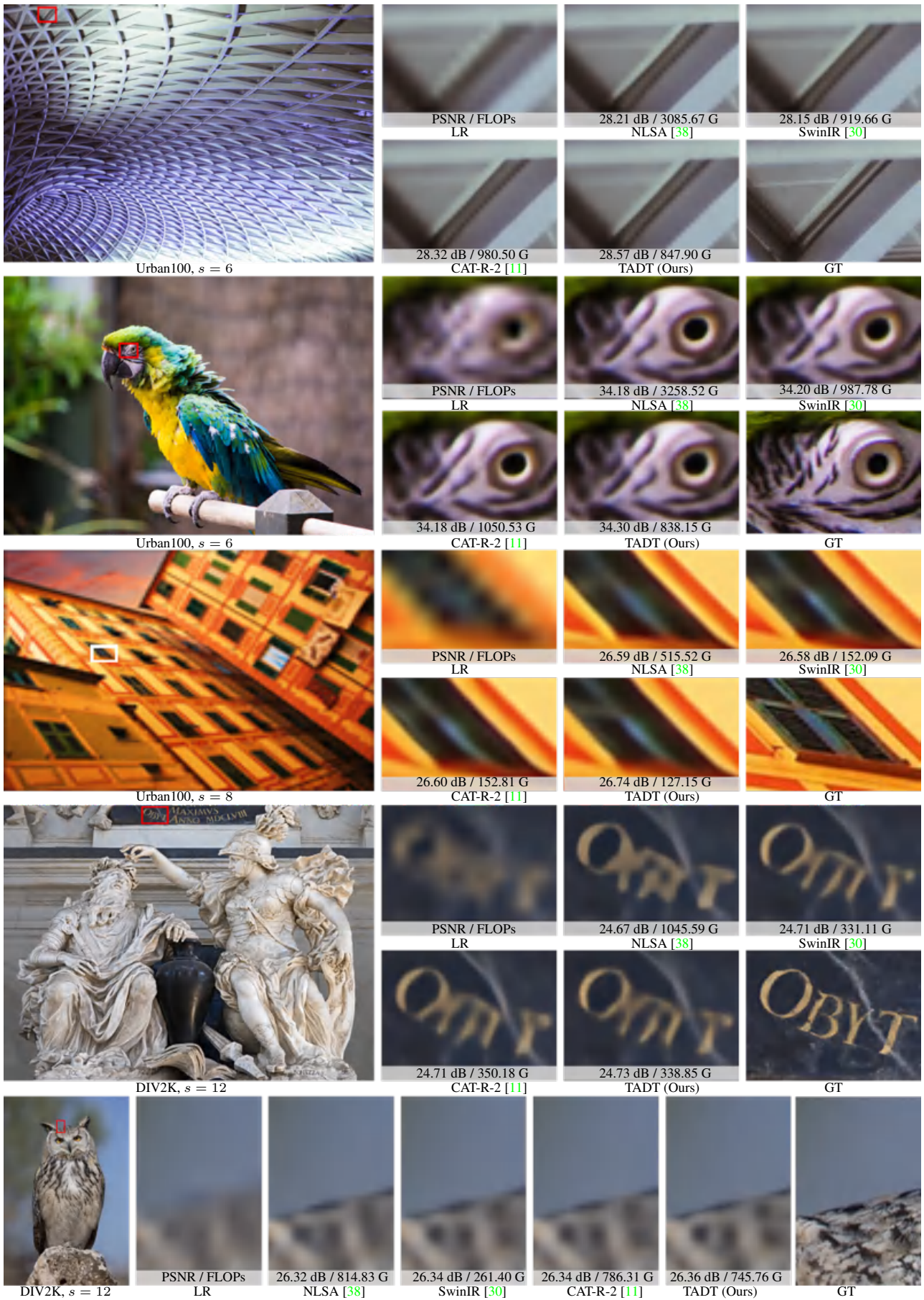


Figure 14. Visual comparison of feature extractors integrated with LTE [27] on super-resolution for natural images at scale 6, 8, 12. The highlighted regions are zoomed in for better view.